

Article

Effect of Oxygen Source on the Various Properties of SnO₂ Thin Films Deposited by Plasma-Enhanced Atomic Layer Deposition

Jong Hyeon Won ¹, Seong Ho Han ², Bo Keun Park ², Taek-Mo Chung ² and Jeong Hwan Han ^{1,*}

¹ Department of Materials Science and Engineering, Seoul National University of Science and Technology, Seoul 01811, Korea; jwon@seoultech.ac.kr

² Division of Advanced Materials, Korea Research Institute of Chemical Technology (KRICT), 141 Gajeong-Ro, Yuseong-Gu, Daejeon 34114, Korea; warhan11@kRICT.re.kr (S.H.H.); parkbk@kRICT.re.kr (B.K.P.); tmchung@kRICT.re.kr (T.-M.C.)

* Correspondence: jhan@seoultech.ac.kr

Received: 13 June 2020; Accepted: 14 July 2020; Published: 18 July 2020



Abstract: Herein, we performed a comparative study of plasma-enhanced atomic layer deposition (PEALD) of SnO₂ films using Sn(dmamp)₂ as the Sn source and either H₂O plasma or O₂ plasma as the oxygen source in a wide temperature range of 100–300 °C. Since the type of oxygen source employed in PEALD determines the growth behavior and resultant film properties, we investigated the growth feature of both SnO₂ PEALD processes and the various chemical, structural, morphological, optical, and electrical properties of SnO₂ films, depending on the oxygen source. SnO₂ films from Sn(dmamp)₂/H₂O plasma (SH-SnO₂) and Sn(dmamp)₂/O₂ plasma (SO-SnO₂) showed self-limiting atomic layer deposition (ALD) growth behavior with growth rates of ~0.21 and 0.07–0.13 nm/cycle, respectively. SO-SnO₂ films showed relatively larger grain structures than SH-SnO₂ films at all temperatures. Interestingly, SH-SnO₂ films grown at high temperatures of 250 and 300 °C presented porous rod-shaped surface morphology. SO-SnO₂ films showed good electrical properties, such as high mobility up to 27 cm² V⁻¹·s⁻¹ and high carrier concentration of ~10¹⁹ cm⁻³, whereas SH-SnO₂ films exhibited poor Hall mobility of 0.3–1.4 cm² V⁻¹·s⁻¹ and moderate carrier concentration of 1 × 10¹⁷–30 × 10¹⁷ cm⁻³. This may be attributed to the significant grain boundary and hydrogen impurity scattering.

Keywords: SnO₂ film; plasma-enhanced atomic layer deposition; oxygen source; H₂O plasma; O₂ plasma; Sn(dmamp)₂

1. Introduction

Tin(IV) oxide (SnO₂) has received considerable research attention due to its excellent electrical conductivity, optical transparency, and chemical stability. This has been extensively utilized in various applications, such as gas sensors, batteries, fuel cells, photovoltaic cells, photodetectors, transparent electronics, and thin film transistors (TFT) [1–7]. For the growth of high-quality SnO₂ thin films, a variety of methods, such as sputtering [8], chemical vapor deposition [9], spray pyrolysis [10], pulsed laser deposition [11], and atomic layer deposition (ALD) [12], have been employed. In particular, the exploitation of ALD SnO₂ films for state-of-the-art devices is increasing because ALD can produce dense, uniform, and conformal films on complex three-dimensional substrates at relatively low deposition temperatures [13]. To obtain high-quality ALD SnO₂ film at wide process temperatures, various Sn precursors, including Sn halides and metal–organic Sn-precursors in combination with different co-reactants, like H₂O, O₃, H₂O₂, and other plasma oxygen sources, have been investigated. Especially, plasma-enhanced atomic layer deposition (PEALD) of SnO₂, in which highly reactive radicals

are employed as co-reactants, has distinct advantages over thermal SnO₂ ALD, e.g., higher growth rates, better film quality, lower impurity concentration, and wider and lower deposition temperature window enabling to grow SnO₂ on low-temperature compatible substrates, like polyethylene naphthalate (PEN), polyethylene terephthalate (PET), and other organic containing materials [14]. Moreover, PEALD, using a highly reactive plasma, extends the choice of precursors by allowing the use of less-reactive precursors, which facilitates the growth of thin films that are difficult to deposit with thermal ALD. Wang et al. reported the low-temperature (~100 °C) SnO₂ PEALD process using tetrakis(dimethylamino)tin (TDMASn) and O₂ plasma at a high growth rate of 0.17 nm/cycle, and a highly efficient perovskite solar cell was demonstrated using 100 °C-deposited SnO₂ as an electron-selective layer [15]. Lee et al. explored SnO₂ PEALD using halogenated SnCl₄ precursor and O₂ plasma. This showed improved growth rate, film purity, and crystallinity compared with the thermal ALD process using SnCl₄/H₂O [16]. However, there is still a lack of precursor combinations for the growth of ALD SnO₂ film at broad temperature window.

Therefore, in this study, we investigated the growth behaviors and film characteristics of PEALD SnO₂ thin films obtained from dimethylamino-2-methyl-2-propoxy-tin(II) (Sn(dmamp)₂) as a Sn precursor and either H₂O plasma or O₂ plasma as the oxygen source. The chemical, optical, structural, and electrical properties of PEALD SnO₂ films, as well as growth features, like self-limiting reaction and growth rate, were characterized depending on the oxygen source over a wide growth temperature range between 100 and 300 °C. In particular, the use of H₂O plasma for PEALD SnO₂ growth has not been reported yet, and PEALD SnO₂ films showed excellent properties of high deposition rate, excellent crystallinity, and low impurity concentration.

2. Experiment

PEALD of SnO₂ films was carried out over a wide temperature range from 100 to 300 °C. SnO₂ films were deposited by using different Sn precursor/reactant combinations of Sn(dmamp)₂/H₂O plasma (SH-SnO₂) and Sn(dmamp)₂/O₂ plasma (SO-SnO₂) separately. The Sn precursor was transported into the chamber by using N₂ (99.9999%) carrier gas of 100 sccm from a bubbler-type canister heated at 60 °C. The gas line for the Sn precursor was maintained at 90 °C to prevent precursor condensation. Deionized H₂O was supplied to create H₂O plasma from a vapor-type canister at 25 °C. O₂ gas (99.999%, 100 sccm) was introduced to produce the O₂ plasma reactant. For all experiments, Si and soda-lime glass were used as substrates. All the SnO₂ PEALD processes were performed over typical four sequential steps: Sn precursor pulse, N₂ purge (10 s, 500 sccm), plasma reactant pulse, and N₂ purge (10 s, 500 sccm). The optimized source and reactant pulse lengths were determined separately for each PEALD process.

The thickness and refractive index of the PEALD SnO₂ films were determined by ex situ ellipsometry system (FS-1, Film sense, Lincoln, Dearborn, MI, USA) at a wavelength of 635 nm. X-ray photoelectron spectroscopy (XPS, K-Alpha, Thermo Scientific, Waltham, MA, USA) surface analysis was performed to indicate the chemical binding states of the elements and to examine the C and N impurity concentrations. Dynamic secondary ion mass spectrometry (D-SIMS, IMS-4FE7, CAMECA, Gennevilliers, France) was performed to examine the H impurity concentration in the SnO₂ films via depth profiling. Ultraviolet–visible spectroscopy (UV–Vis, sepcord200, analytikjena, Jena, Germany) was performed to estimate transmittance and optical band gap of the SnO₂ films. Surface morphologies of the SH-SnO₂ and SO-SnO₂ films grown at various temperatures were observed using high-resolution field-emission scanning electron microscopy (HR-FESEM, SU8010, Hitach, Tokyo, Japan). Film crystallinity of the SnO₂ thin films was investigated using glancing-angle X-ray diffraction (GAXRD, D-MAX 2500, Rigaku, Tokyo, Japan). Finally, electrical properties, like carrier concentration, mobility, and resistivity of the SnO₂ films on soda-lime glass, were measured by Hall-effect measurements (HMS-3000, ecopia, Anyang, South Korea).

3. Results and Discussion

Figure 1a,b shows the growth characteristics of PEALD SH-SnO₂ and SO-SnO₂ at a deposition temperature of 200 °C. Figure 1a shows the change in the growth per cycle (GPC) of the SH-SnO₂ and SO-SnO₂ films by varying the Sn precursor and reactant pulse lengths. For SH-SnO₂, it was found that a Sn precursor pulse length of >5 s and H₂O plasma pulse length of >3 s were required to obtain the saturated GPC with self-limiting surface reaction. The optimized pulse condition was determined to be as follows: Sn precursor pulse of 6 s, N₂ purge for 10 s, H₂O plasma reactant pulse of 5 s, and N₂ purge for 10 s. SO-SnO₂ PEALD also showed the self-saturated growth characteristics for the Sn precursor and O₂ plasma pulse lengths of >4 s and >3 s, respectively. As depicted in Figure 1b, both SnO₂ PEALD processes show the linear increase in film thickness with increasing number of ALD cycles, and the estimated GPCs of SH-SnO₂ and SO-SnO₂ films are approximately 0.21 and 0.08 nm/cycle, respectively. The obtained GPC of SH-SnO₂ was much higher than that of SO-SnO₂ PEALD and those of previously reported SnO₂ ALD from Sn(dmamp)₂/O₃ (0.018–0.042 nm/cycle), tetraethyltin/H₂O₂ (0.073–0.083 nm/cycle), Sn(edpa)₂/O₂ plasma (0.070 nm/cycle), TDMASn/O₃ (0.10–0.16 nm/cycle), and Sn(acac)₃/O₃ (0.10 nm/cycle) [17–21]. The high GPC of SH-SnO₂ PEALD might originate from the high reactivity of H₂O plasma and the high density of accessible reactive sites on the surface after H₂O plasma pulse. Tarlov et al. found that H₂O plasma treatment on SnO₂ film induced a hydroxylated surface, which may in turn act as reactive sites for subsequent Sn precursor chemisorption [22,23]. In addition, Kawamura et al. reported higher reactivity of H₂O plasma than that of O₂ plasma in ZnO ALD process [24].

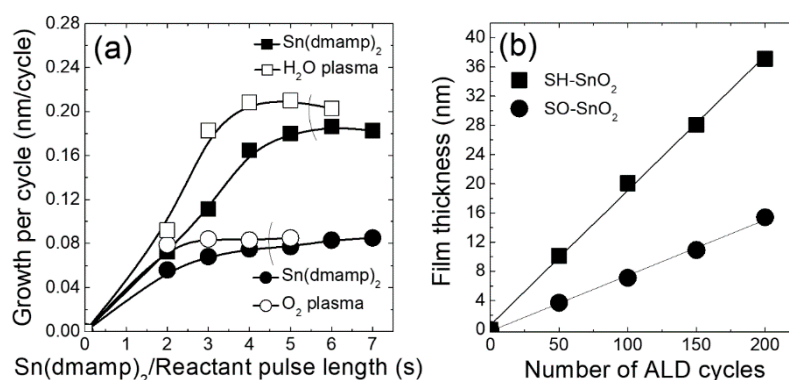


Figure 1. (a) Variations in the growth per cycle (GPC) of SH-SnO₂ and SO-SnO₂ plasma-enhanced atomic layer deposition (PEALD) processes at 200 °C, depending on the Sn source and reactant pulse lengths. (b) Change in SnO₂ thicknesses with increasing number of SH-SnO₂ and SO-SnO₂ PEALD cycles.

Figure 2 shows the variations of the GPC and refractive indices of the SH-SnO₂ and SO-SnO₂ films as functions of deposition temperatures ranging from 100 to 300 °C. SH-SnO₂ films showed a constant GPC of 0.21 nm/cycle at a wide temperature range of 100–300 °C. Refractive indices of SH-SnO₂ films deposited at 100–300 °C were examined by using an ellipsometer at a wavelength of 633 nm. At the low-temperature range of 100–200 °C, the refractive index of SH-SnO₂ films was 1.9, comparable with that of reported SnO₂ films (1.9–2.0) [25–27]. By contrast, the refractive index values at the high-temperature range of 250–300 °C showed an abrupt decrease to 1.55 with increasing growth temperatures, implying the formation of less-dense SH-SnO₂ films. The lower refractive index at higher deposition temperature was unexpected because previous studies reported that the density of ALD SnO₂ films generally increased with deposition temperature [25,26]. The deposition of less-dense SH-SnO₂ films will be discussed in detail later. For SO-SnO₂ films, the GPC of 0.071–0.087 nm/cycle was obtained in the ALD temperature window of 150–250 °C. At deposition temperatures of 100 and 300 °C, the GPC values were higher than those at 150–250 °C probably due to condensation of

$\text{Sn}(\text{dmamp})_2$ precursor and enhanced reaction kinetics between $\text{Sn}(\text{dmamp})_2$ and O_2 plasma at 100 and 300 °C, respectively. The SO- SnO_2 films showed higher GPC values than those of SnO_2 films obtained from the same $\text{Sn}(\text{dmamp})_2$ precursor and O_3 (0.017–0.042 nm/cycle) [17]. Compared with SH- SnO_2 , the SO- SnO_2 films exhibited high refractive index values of 1.9–2.0 at all deposition temperatures, indicating the formation of dense SnO_2 films irrespective of deposition temperature.

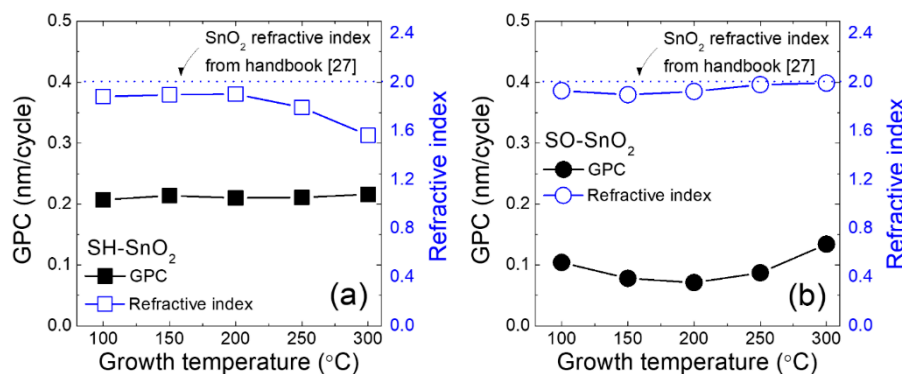


Figure 2. GPC and refractive index of the SnO_2 thin films deposited at 100–300 °C using (a) $\text{Sn}(\text{dmamp})_2/\text{H}_2\text{O}$ plasma and (b) $\text{Sn}(\text{dmamp})_2/\text{O}_2$ plasma.

Although O_2 plasma has been extensively employed as an oxidizing agent in ALD and other thin-film deposition processes, the role of H_2O plasma in ALD process is still unclear because H_2O plasma contains the reductive species of H_2 , H^* , and H^+ , as well as the oxidative species of O_2 , O^* , and OH [28]. Besides, Stuckert et al. and Choi et al. reported that H_2O plasma treatment on SnO_2 surface resulted in the reduction of SnO_2 to metallic Sn, implying that H_2O plasma can act as a reducing agent rather than as an oxidant [29,30]. In contrast, some previous reports on PEALD processes revealed that H_2O plasma could be utilized as an oxidizing co-reactant for the growth of ZnO and TiO_2 films [24,31]. Therefore, the chemical binding states and oxygen concentrations of SH- SnO_2 and SO- SnO_2 films must be investigated to identify the surface reaction that occurred herein. To examine the chemical binding state of both SnO_2 films, XPS analysis was performed (Figure 3a,b). Sn 3d core-level XP spectra showed that the Sn 3d_{5/2} peaks from both PEALD films were almost identical at 486.5–486.7 eV, irrespective of the deposition temperature. This suggests the growth of pure SnO_2 films (+4 oxidation state) without other sub-valent oxide phases, such as Sn_2O_3 , SnO, and Sn, and that H_2O plasma acted as an oxidizing agent rather than as a reducing agent. To measure the concentration of residual carbon and nitrogen impurities that may come from the Sn precursor, N 1s and C 1s spectra were also obtained. For SH- SnO_2 films, carbon and nitrogen concentrations were below XPS detection levels at all investigated deposition temperatures. Contrarily, carbon impurities were detected for SO- SnO_2 films grown at a low temperature of 100 °C, as shown in the inset of Figure 3b, attributed to the comparably lower reactivity of O_2 plasma than H_2O plasma.

Further chemical analysis was performed using D-SIMS, and the Sn/O ratios and hydrogen concentrations of SH- SnO_2 and SO- SnO_2 films deposited at 200 °C were compared. Figure 4a,b shows the compositional depth profiles of the SH- SnO_2 and SO- SnO_2 films, respectively. Both PEALD SnO_2 films showed uniform Sn, O, and H distributions in the depth direction. Furthermore, the Sn/O intensity ratios for both SnO_2 films were perfectly identical, suggesting that the SnO_2 films had the same Sn:O compositions. Meanwhile, the SH- SnO_2 film showed two-fold higher hydrogen intensity than that of the SO- SnO_2 film due to hydrogen incorporation from H-containing species in H_2O plasma. Notably, hydrogen impurity concentrations in various oxides influence the crystalline structure and electrical properties, like carrier mobility and concentrations [32–34]. For example, Husein et al. reported that hydrogen-doped indium oxide films showed decreased electron mobility as the hydrogen content was increased to 5.7% [33].

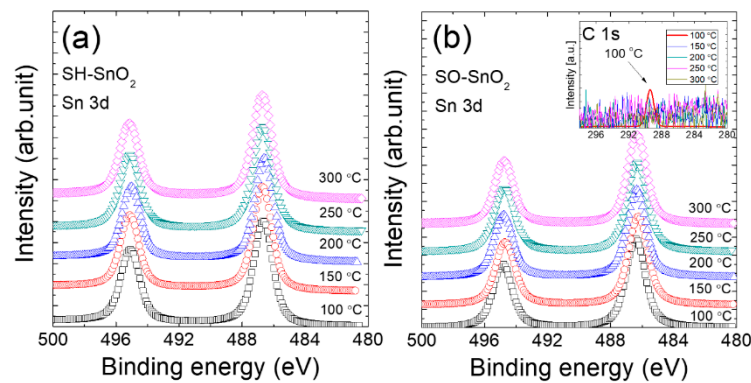


Figure 3. Sn 3d XPS core level spectra of the SnO₂ films deposited at 100–300 °C using (a) Sn(dmamp)₂/H₂O plasma and (b) Sn(dmamp)₂/O₂ plasma. Inset of Figure 3b shows the C 1s X-ray photoelectron (XP) spectra of SO-SnO₂ films.

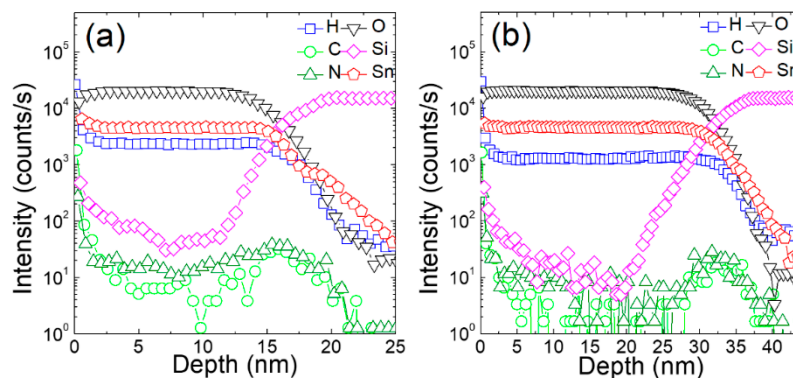


Figure 4. Dynamic secondary ion mass spectrometry (D-SIMS) depth profiles of (a) SH-SnO₂ and (b) SO-SnO₂ films deposited at 200 °C.

Figure 5 shows the optical properties of the SH-SnO₂ and SO-SnO₂ films grown at different deposition temperatures. Figure 5a,b presents the transmittance of the 20-nm-thick PEALD SH-SnO₂ and SO-SnO₂ films deposited on soda-lime glass, respectively. It was shown that all the SnO₂ films have high transparencies (>80%) in the visible light range (wavelength = 350–700 nm). Figure 5c,d exhibits the optical band gaps of the SnO₂ films derived from the Tauc equation ($\alpha hv = A (hv - E_g)^{1/2}$ for direct band gap transition, where α is the absorption coefficient, hv is the photon energy, and E_g is the optical band gap) [35,36]. Optical band gaps of the SnO₂ films were determined by extrapolating the graph of the linear part of the curve to the x -axis. It was confirmed that the band gap energy, regardless of the deposition temperature and plasma reactant, was almost constant at about 3.95–3.98 eV, which is in good agreement with ALD SnO₂ films [7].

The crystalline structures of the 20-nm-thick SnO₂ films were investigated at different deposition temperatures ranging from 100 to 300 °C. For SH-SnO₂ films, distinct diffraction peaks corresponding to tetragonal rutile SnO₂ (110), SnO₂ (101), and SnO₂ (200) were found at 26.5°, 34.0°, and 38.5° over a wide deposition temperature range of 100–300 °C, indicating the growth of polycrystalline SnO₂ films (Figure 6a). The SH-SnO₂ films grown at lower temperatures of 100–200 °C showed the (101) preferred orientation, while a strong (110) preferred orientation was found by increasing the deposition temperature to 300 °C. For SO-SnO₂ (Figure 6b), the clear diffraction peaks at 26.5° and 38° for tetragonal SnO₂ (110) and SnO₂ (200), respectively, were observed at deposition temperatures of >150 °C. The SO-SnO₂ films showed the (110) preferred orientation, irrespective of the deposition temperature. By contrast, amorphous SnO₂ film was grown at 100 °C. By contrast to SH-SnO₂, the weak diffraction peak at 24.8°, which corresponds to orthorhombic columbite SnO₂ (110), was observed for

SO-SnO₂, and the relative intensity of orthorhombic SnO₂ peak increases with growth temperature. It should be noted that the growth of less-stable orthorhombic SnO₂ by ALD has been rarely reported. Kim et al. observed an orthorhombic SnO₂ phase by epitaxial PEALD on yttria-stabilized zirconia substrate [37].

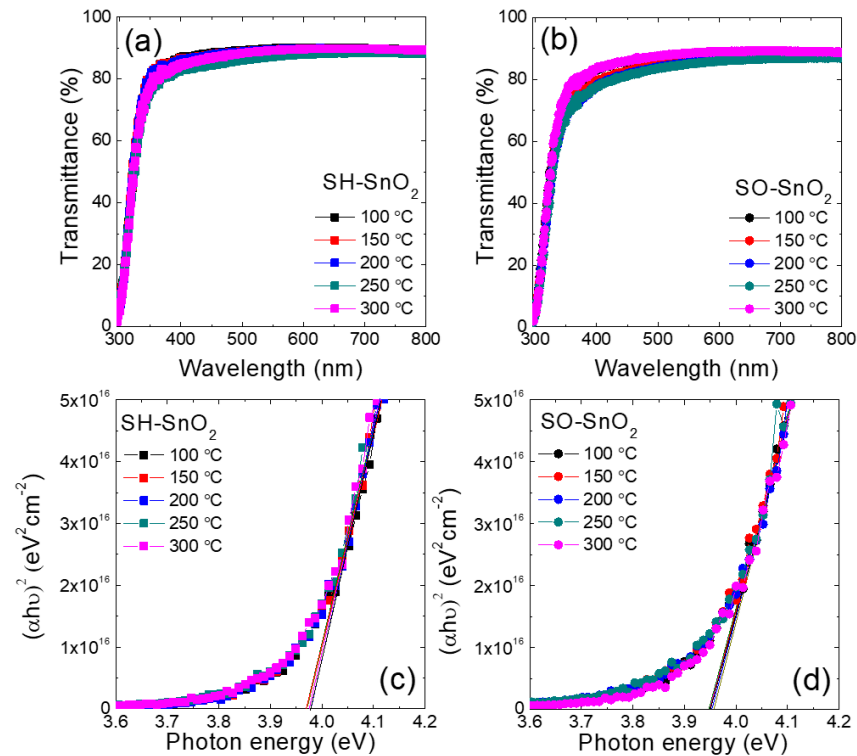


Figure 5. Optical transmittance of 20-nm-thick (a) SH-SnO₂ films and (b) SO-SnO₂ films deposited on a soda-lime glass substrate at 100–300 °C. Optical band gaps of (c) SH-SnO₂ and (d) SO-SnO₂ films grown at 100–300 °C.

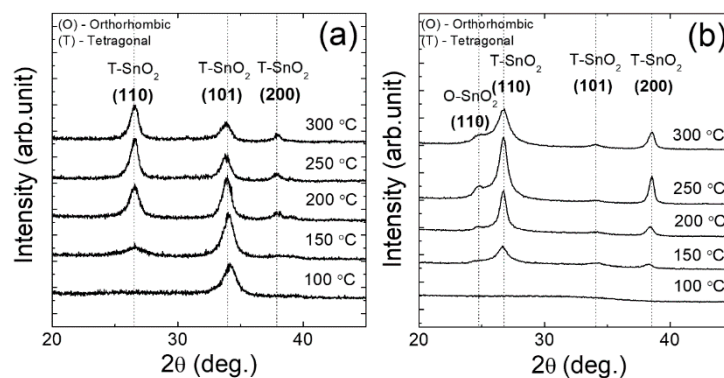


Figure 6. Glancing-angle X-ray diffraction (GAXRD) patterns of (a) SH-SnO₂ and (b) SO-SnO₂ thin films deposited at different temperatures of 100, 150, 200, 250, and 300 °C.

Figure 7a shows the plane-view high-resolution FESEM images of the SH-SnO₂ films deposited at 100–300 °C. Despite the low deposition temperature of 100 °C, the SH-SnO₂ film showed a small and dense nanocrystalline structure. At deposition temperatures up to 200 °C, the grain size of the SH-SnO₂ films were approximately 15–20 nm, and a dense SnO₂ surface was observed. By contrast, SnO₂ films became less dense and rougher on increasing the temperature beyond 250 °C, and eventually the SH-SnO₂ films showed significantly porous structures with rod-shaped crystallites at 300 °C.

The formation of porous nanostructured SnO₂ is consistent with the noticeably low refractive index of the SH-SnO₂ films grown at 250 °C and 300 °C. Although it is very tricky to reveal the complicated surface reactions during PEALD of SH-SnO₂, the morphology change of the SnO₂ films from smooth SnO₂ surface to rod-shaped porous structure at deposition temperatures of >250 °C might be ascribed to the partial reduction of SnO₂ to Sn metal by reductive H-containing species in H₂O plasma, followed by thermal etching via Sn evaporation or agglomeration of the Sn metal. It has been reported that H₂O plasma treatment on SnO₂ film resulted in a morphological change to nanoglobular structure due to reduction of SnO₂ to Sn [29]. At the higher growth temperature of >350 °C, SH-SnO₂ resulted in more porous surface due to much severe reduction of SnO₂ and Sn evaporation/agglomeration (data not shown here). Figure 7b shows the plane-view images of the SO-SnO₂ films grown at temperatures of 100–300 °C. The SO-SnO₂ film grown at 100 °C showed an amorphous phase and merely a few crystallites scattered in the amorphous film. On increasing the deposition temperature to 250 °C, the SO-SnO₂ films showed dense and large polygonal grains of size ~50 nm, while the SO-SnO₂ film grown at 300 °C showed a dense and polycrystalline structure with decreased grain size. The formation of dense SO-SnO₂ thin films at deposition temperatures of 250 °C and 300 °C is well matched with the high refractive index of ~2.0 obtained from an ellipsometer.

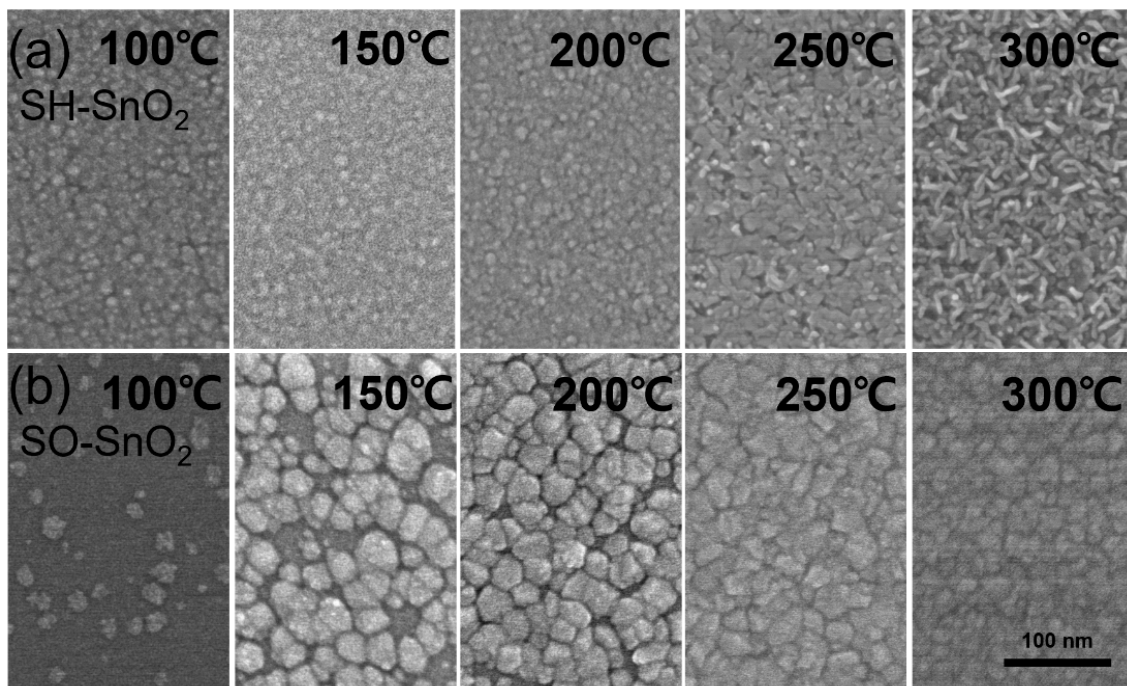


Figure 7. Plane-view high-resolution FESEM images of (a) SH-SnO₂ and (b) SO-SnO₂ films grown at deposition temperatures of 100–300 °C.

Hall-effect measurements were performed to investigate the electrical properties of the PEALD of SnO₂ films at room temperature. SnO₂ films (20-nm thick) were deposited on soda-lime glass using both H₂O plasma and O₂ plasma at 100–300 °C, and indium was used for the ohmic contact on the four vertexes. First, it was confirmed that all the PEALD SnO₂ films exhibited n-type carrier behavior, i.e., the majority carrier was electrons, regardless of the deposition temperature. Figure 8a,b shows the carrier concentrations, Hall mobilities, and resistivities of the SH-SnO₂ and SO-SnO₂ films, respectively. SH-SnO₂ films grown at 100–300 °C have moderate carrier concentration of approximately 1×10^{17} – 30×10^{17} cm⁻³ and rather low electrical mobility of 0.4–1.5 cm² V⁻¹·s⁻¹. The low Hall mobilities of the SH-SnO₂ thin films could be explained by the significant grain boundary scattering due to the small grain structure and high grain boundary density, as observed in the FESEM images. Resistivities of the SH-SnO₂ films grown at 100–150 °C were ~5 Ω·cm, and it gradually increased

to 7–38 $\Omega\cdot\text{cm}$ for the SH-SnO₂ films grown at 200–300 °C, attributed to the porous SnO₂ structures (Figure 7a). For polycrystalline SO-SnO₂ films grown at 100–300 °C, higher carrier concentrations of 7×10^{18} – 4×10^{19} cm^{-3} were obtained. The SO-SnO₂ films grown at 100 °C showed Hall mobilities of ~ 5.8 $\text{cm}^2 \text{V}^{-1}\cdot\text{s}^{-1}$, which continually increased to 27 $\text{cm}^2 \text{V}^{-1}\cdot\text{s}^{-1}$ as the deposition temperature was raised to 250 °C, along with the lowest resistivity of 6×10^{-3} $\Omega\cdot\text{cm}$. This was evidenced by the larger and denser grains obtained at the high deposition temperature of 250 °C.

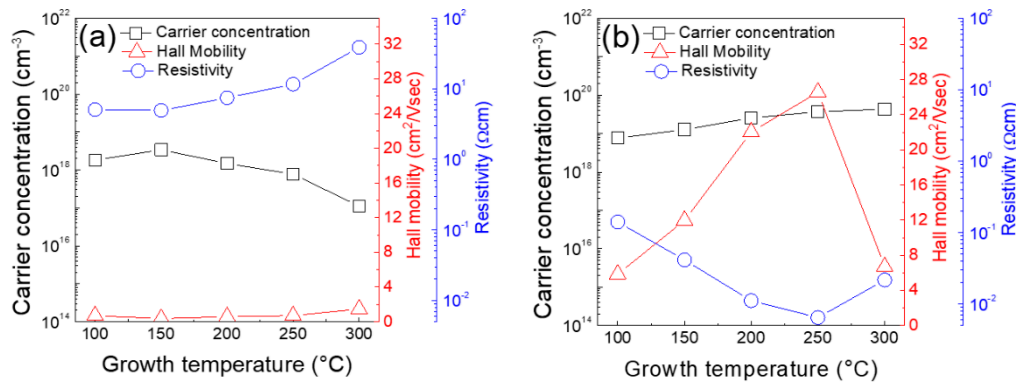


Figure 8. Carrier concentrations, Hall mobilities, and resistivities of (a) SH-SnO₂ and (b) SO-SnO₂ films as a function of growth temperature.

4. Conclusions

In this study, SnO₂ PEALD processes over a wide growth temperature range of 100–300 °C using different plasma sources, either H₂O plasma or O₂ plasma, were demonstrated, and their growth behavior and film properties were compared. SnO₂ films grown from H₂O plasma (SH-SnO₂) showed a higher growth rate of 0.21 nm/cycle than that of SnO₂ films grown from O₂ plasma (SO-SnO₂) due to the stronger reactivity of H₂O plasma and more OH-reactive sites. The SH-SnO₂ films showed negligible carbon and nitrogen impurities at all deposition temperatures from 100 to 300 °C, but they contained two-fold higher hydrogen concentrations than the SO-SnO₂ films. The SO-SnO₂ featured dense and uniform surface morphology with relatively larger grain size, while SH-SnO₂ showed nanocrystallites with small grain size at moderate temperatures, and porous rod-shaped structures at higher deposition temperatures of 250 and 300 °C. At 250 °C, the SO-SnO₂ film showed high carrier concentration of $\sim 4 \times 10^{19}$ cm^{-3} and high Hall mobility of 27 $\text{cm}^2 \text{V}^{-1}\cdot\text{s}^{-1}$. By contrast, the SH-SnO₂ films showed poorer conductivity, lower carrier concentration, and lower Hall mobility than the SO-SnO₂ films at all deposition temperatures, probably due to the significant grain boundary scattering and hydrogen impurity scattering within the SH-SnO₂ films.

Author Contributions: Conceptualization, J.H.W. and J.H.H.; investigation, J.H.W. and J.H.H.; resources, S.H.H., B.K.P. and T.-M.C.; writing—original draft preparation, J.H.W. and J.H.H.; writing—review and editing, J.H.W. and J.H.H.; supervision, J.H.H.; project administration, J.H.H. All authors have read and agreed to the published version of the manuscript.

Funding: This study was supported by the Research Program funded by the SeoulTech (Seoul National University of Science and Technology).

Conflicts of Interest: The authors declare no conflict of interest.

References

1. Paulowicz, I.; Hrkac, V.; Kaps, S.; Cretu, V.; Lupan, O.; Braniste, T.; Duppel, V.; Tiginyanu, I.; Kienle, L.; Adelung, R. Three-dimensional SnO₂ nanowire networks for multifunctional applications: From high-temperature stretchable ceramics to ultra responsive sensors. *Am. Ceram. Soc. Bull.* **2015**, *94*, 21.
2. Guan, C.; Wang, X.; Zhang, Q.; Fan, Z.; Zhang, H.; Fan, H.J. Highly stable and reversible lithium storage in SnO₂ nanowires surface coated with a uniform hollow shell by atomic layer deposition. *Nano Lett.* **2014**, *14*, 4852–4858. [[CrossRef](#)]
3. Kim, D.H.; Shin, D.Y.; Lee, Y.G.; An, G.H.; Han, J.H.; Ahn, H.J.; Choi, B.J. Effects of SnO₂ layer coated on carbon nanofiber for the methanol oxidation reaction. *Ceram. Int.* **2018**, *44*, 19554–19559. [[CrossRef](#)]
4. Park, M.; Kim, J.Y.; Son, H.J.; Lee, C.H.; Jang, S.S.; Ko, M.J. Low-temperature solution-processed Li-doped SnO₂ as an effective electron transporting layer for high-performance flexible and wearable perovskite solar cells. *Nano Energy* **2016**, *26*, 208–215. [[CrossRef](#)]
5. Chu, H.C.; Shen, Y.S.; Hsieh, C.H.; Huang, J.H.; Wu, Y.H. Low-voltage operation of ZrO₂-gated n-type thin-film transistors based on a channel formed by hybrid phases of SnO and SnO₂. *ACS Appl. Mater. Interfaces* **2015**, *7*, 15129–15137. [[CrossRef](#)]
6. Jarzebski, Z.M.; Marton, J.P. Physical properties of SnO₂ materials. *J. Electrochem. Soc.* **1976**, *123*, 299–310. [[CrossRef](#)]
7. Manificier, J.C.; De Murcia, M.; Fillard, J.P.; Vicario, E. Optical and electrical properties of SnO₂ thin films in relation to their stoichiometric deviation and their crystalline structure. *Thin Solid Films* **1977**, *41*, 127–135. [[CrossRef](#)]
8. Minami, T.; Nanto, H.; Takata, S. Highly conducting and transparent SnO₂ thin films prepared by RF magnetron sputtering on low-temperature substrates. *Jpn. J. Appl. Phys.* **1988**, *27*, L287–L289. [[CrossRef](#)]
9. Liu, Y.; Koep, E.; Liu, M. A highly sensitive and fast-responding SnO₂ sensor fabricated by combustion chemical vapor deposition. *Chem. Mater.* **2005**, *17*, 3997–4000. [[CrossRef](#)]
10. Korotcenkov, G.; Brinzari, V.; Schwank, J.; Dibattista, M.; Asiliev, A. Peculiarities of SnO₂ thin film deposition by spray pyrolysis for gas sensor application. *Sens. Actuators B* **2001**, *77*, 244–252. [[CrossRef](#)]
11. Kim, H.; Piqué, A. Transparent conducting Sb-doped SnO₂ thin films grown by pulsed-laser deposition. *Appl. Phys. Lett.* **2004**, *218*, 10–13.
12. Lu, J.; Sundqvist, J.; Ottosson, M.; Tarre, A.; Rosental, A.; Aarik, J.; Hårsta, A. Microstructure characterisation of ALD-grown epitaxial SnO₂ thin films. *J. Cryst. Growth.* **2004**, *260*, 191–200. [[CrossRef](#)]
13. George, S.M. Atomic layer deposition: An overview. *Chem. Rev.* **2010**, *110*, 111–131. [[CrossRef](#)] [[PubMed](#)]
14. Johnson, R.W.; Hultqvist, A.; Bent, S.F. A brief review of atomic layer deposition: From fundamentals to applications. *Mater. Today.* **2014**, *17*, 236–246. [[CrossRef](#)]
15. Wang, C.; Zhao, D.; Grice, C.R.; Liao, W.; Yu, Y.; Cimaroli, A.; Shrestha, N.; Roland, P.J.; Chen, J.; Yu, Z.; et al. Low-temperature plasma-enhanced atomic layer deposition of tin oxide electron selective layers for highly efficient planar perovskite solar cells. *J. Mater. Chem. A.* **2016**, *4*, 12080–12087. [[CrossRef](#)]
16. Lee, D.K.; Wan, Z.; Bae, J.S.; Lee, H.B.R.; Ahn, J.H.S.; Kim, D.; Kim, J.; Kwon, S.H. Plasma-enhanced atomic layer deposition of SnO₂ thin films using SnCl₄ and O₂ plasma. *Mater. Lett.* **2016**, *166*, 163–166. [[CrossRef](#)]
17. Choi, M.J.; Cho, C.J.; Kim, K.C.; Pyeon, J.J.; Park, H.H.; Kim, H.S.; Han, J.H.; Kim, C.G.; Chung, T.M.; Park, T.J.; et al. SnO₂ thin films grown by atomic layer deposition using a novel Sn precursor. *Appl. Surf. Sci.* **2014**, *320*, 188–194. [[CrossRef](#)]
18. Lim, S.S.; Baek, I.H.; Kim, K.C.; Baek, S.H.; Park, H.H.; Kim, J.S.; Kim, S.K. Atomic layer deposition of SnO₂ thin films using tetraethyltin and H₂O₂. *Ceram. Int.* **2019**, *45*, 20600–20605. [[CrossRef](#)]
19. Kim, H.Y.; Nam, J.H.; George, S.M.; Park, J.S.; Park, B.K.; Kim, G.H.; Jeon, D.J.; Chung, T.M.; Han, J.H. Phase-controlled SnO₂ and SnO growth by atomic layer deposition using Bis(N-ethoxy-2,2-dimethyl propanamido)tin precursor. *Ceram. Int.* **2019**, *45*, 5124–5132. [[CrossRef](#)]
20. won Choi, D.; Park, J.S. Highly conductive SnO₂ thin films deposited by atomic layer deposition using tetrakis-dimethyl-amine-tin precursor and ozone reactant. *Surf. Coatings Technol.* **2014**, *259*, 238–243. [[CrossRef](#)]

21. Chang, S.; Selvaraj, S.K.; Choi, Y.-Y.; Hong, S.; Nakhmanson, S.M.; Takoudis, C.G. Atomic layer deposition of environmentally benign SnTiO_x as a potential ferroelectric material. *J. Vac. Sci. Technol. A* **2016**, *34*, 01A119. [[CrossRef](#)]
22. Tarlov, M.J.; Evans, J.F.; Newman, J.G. Static SIMS and XPS study of water plasma exposed tin oxide films. *Appl. Surf. Sci.* **1993**, *64*, 115–125. [[CrossRef](#)]
23. Tarlov, M.J.; Evans, J.F. Surface characterization of radio frequency water plasma treated and annealed polycrystalline tin oxide thin films. *Chem. Mater.* **1990**, *2*, 49–60. [[CrossRef](#)]
24. Kawamura, Y.; Hattori, N.; Miyatake, N.; Uraoka, Y. Comparison between ZnO films grown by plasma-assisted atomic layer deposition using H₂O plasma and O₂ plasma as oxidant. *J. Vac. Sci. Technol. A* **2013**, *31*, 01A142. [[CrossRef](#)]
25. Heo, J.; Kim, S.B.; Gordon, R.G. Atomic layer deposition of tin oxide with nitric oxide as an oxidant gas. *J. Mater. Chem.* **2012**, *22*, 4599–4602. [[CrossRef](#)]
26. Heo, J.; Hock, A.S.; Gordon, R.G. Low temperature atomic layer deposition of tin oxide. *Chem. Mater.* **2010**, *22*, 4964–4973. [[CrossRef](#)]
27. Patnaik, P. *Handbook of Inorganic Chemicals*; McGraw-Hill Companies, Inc.: New York, NY, USA, 2003; p. 940. ISBN 0-07-049439-8.
28. Stuckert, E.P.; Miller, C.J.; Fisher, E.R. Gas-phase diagnostics during H₂ and H₂O plasma treatment of SnO₂ nanomaterials: Implications for surface modification. *J. Vac. Sci. Technol. B* **2017**, *35*, 021802. [[CrossRef](#)]
29. Stuckert, E.P.; Fisher, E.R. Ar/O₂ and H₂O plasma surface modification of SnO₂ nanomaterials to increase surface oxidation. *Sens. Actuators B Chem.* **2015**, *208*, 379–388. [[CrossRef](#)]
30. Choi, M.S.; Lee, Y.J.; Kwon, J.D.; Jeong, Y.; Park, J.Y.; Kang, Y.C.; Song, P.K.; Kim, D.H. Effects of hydrogen plasma treatment on SnO₂:F substrates for amorphous Si thin film solar cells. *Curr. Appl. Phys.* **2013**, *13*, 1589–1593. [[CrossRef](#)]
31. Xie, Q.; Musschoot, J.; Deduytsche, D.; Van Meirhaeghe, R.L.; Detavernier, C.; Van Den Berghe, S.; Jiang, Y.L.; Ru, G.P.; Li, B.Z.; Qu, X.P. Growth kinetics and crystallization behavior of TiO₂ films prepared by plasma enhanced atomic layer deposition. *J. Electrochem. Soc.* **2008**, *155*, 688–692. [[CrossRef](#)]
32. Dymond, E.G. Scattering of electrons in helium. *Nature* **1926**, *118*, 336–337. [[CrossRef](#)]
33. Husein, S.; Stuckelberger, M.; West, B.; Ding, L.; Dazou, F.; Morales-Masis, M.; Duchamp, M.; Holman, Z.; Bertoni, M.I. Carrier scattering mechanisms limiting mobility in hydrogen-doped indium oxide. *J. Appl. Phys.* **2018**, *123*, 245102. [[CrossRef](#)]
34. Villamagua, L.; Stashans, A.; Carini, M.; Maldonado, F. Doping of SnO₂ with H atoms: An alternative way to attain n-type conductivity. *AIP Adv.* **2016**, *6*, 115217. [[CrossRef](#)]
35. Baco, S.; Chik, A.; Yassin, F.M. Study on optical properties of tin oxide thin film at different annealing temperature. *J. Sci. Technol.* **2012**, *4*, 61–72.
36. Tauc, J.C. *Optical Properties of Solid*; Abeles, F., Ed.; North-Holland Publishing: Amsterdam, The Netherlands, 1972; p. 279.
37. Kim, S.; Kim, D.-H.; Hong, S.-H. Epitaxial growth of orthorhombic SnO₂ films on various YSZ substrates by plasma enhanced atomic layer deposition. *J. Cryst. Growth* **2012**, *348*, 15–19. [[CrossRef](#)]

